

# Maximum-Likelihood Deconvolution in the Spatial and Spatial-Energy Domain for Events With Any Number of Interactions

Weiye Wang, *Member, IEEE*, Christopher G. Wahl, *Member, IEEE*, Jason M. Jaworski, *Student Member, IEEE*, and Zhong He, *Senior Member, IEEE*

**Abstract**—In previous works, maximum-likelihood expectation-maximization deconvolution for two-interaction events within a single CdZnTe detector with dimensions of  $1.5\text{ cm} \times 1.5\text{ cm} \times 1\text{ cm}$  was implemented. This deconvolution method is capable of estimating the source image for each energy range as well as the incident spectrum for each direction around the detector. To improve the detection efficiency and the image resolution, we have built a four-detector array system; each detector has dimensions of  $2\text{ cm} \times 2\text{ cm} \times 1.5\text{ cm}$ . Using this detector-array system, from a Co-60 measurement, 41.5% of recorded events in the energy window from 1100 keV to 1200 keV are two-interaction events. The goal of this work is to increase the efficiency of this deconvolution algorithm by extending the calculation of the system response functions to events with other number of interactions. We first analytically extend the system response function calculation to three-interaction events by deriving the probability density function, considering the measurement noise, and integrating over the digitization and pixelation volume. The system response function is then simplified, modularized, and extrapolated to events with other numbers of interactions from an array system. By including events with any number of interactions in the system model, imaging makes use of all recorded events, and the angular resolution is improved. This deconvolution algorithm is applicable to any gamma-ray detector system that has the capability of recording 3D interaction location and energy deposition for each interaction.

**Index Terms**—Cadmium zinc telluride, Compton camera, detector array, image reconstruction, maximum likelihood expectation maximization, system response function.

## I. INTRODUCTION

**T**RADITIONAL spectroscopic gamma-ray detectors record the total energy deposited by a gamma ray in the active volume, producing a single energy spectrum. However, when the three-dimensional gamma-ray interaction positions in the detector can be recorded, one can also produce an image of the source intensity around the detector using Compton imaging. A simple back-projection image can be achieved by

summing up the back-projection cones in the image space. The limited angular resolution of the simple back-projection method has been well documented [1]. Maximum-likelihood deconvolution can give better angular resolution by considering the probabilities that each measured event was produced by a photon originating from each direction in space [1], [2]. By performing this deconvolution in a combined spatial-energy domain and including Compton-continuum events in the system model, the maximum-likelihood expectation-maximization method estimates the source distribution at each incident energy as well as the true incident spectrum in each specific direction free of Compton continuum. Previously, the probabilities used in the system response function have been derived for two-interaction events in one detector [3]. Here we generalize the system response function calculation for two-interaction events to an array of detectors.

This array system uses multiple three-dimensional-position-sensitive room-temperature CdZnTe detectors, each with dimensions of  $2\text{ cm} \times 2\text{ cm} \times 1.5\text{ cm}$ . It improves detection efficiency for high-energy photons as well as angular resolution [4]. All detectors in the array system trigger together, so interactions from a single incident photon that span multiple detector modules can be read out simultaneously.

With the array system, low-energy gamma rays primarily produce single-interaction events, while higher energy gamma rays primarily produce multiple-interaction events, with three- and four-interaction events contributing to a large fraction of the recorded events. In order to make use of these events and improve the imaging efficiency, the system response functions are also extended to all events with any number of interactions occurring in the detector-array system. These system response functions are applicable to any gamma-ray detector capable of recording the energies and positions of interaction locations.

In this paper, the probability of three-interaction events is analytically derived and simplified. The system response function is then modularized and extrapolated to events with any number of interactions. Experimental imaging performance is shown for the newly derived system response functions, and the statistical uncertainty of this algorithm is presented.

## II. SYSTEM RESPONSE FUNCTION FOR THREE-INTERACTION EVENTS IN A DETECTOR-ARRAY SYSTEM

The system response function  $t_{ij}$  is defined as the probability that a photon with a certain incident energy  $E_0$  from a certain spatial direction (image pixel), defined as  $j$ , creates an event

Manuscript received May 10, 2011; revised December 11, 2011; accepted December 22, 2011. Date of publication February 29, 2012; date of current version April 13, 2012. This work was supported by the Department of Energy (DOE) NA-22 Office.

The authors are with the Department of Nuclear Engineering and Radiological Sciences, University of Michigan, Ann Arbor, MI 48109 USA (e-mail: wywang@umich.edu; cgwahl@umich.edu; jasonjaw@umich.edu; hezhong@umich.edu).

Color versions of one or more of the figures in this paper are available online at <http://ieeexplore.ieee.org>.

Digital Object Identifier 10.1109/TNS.2012.2183384

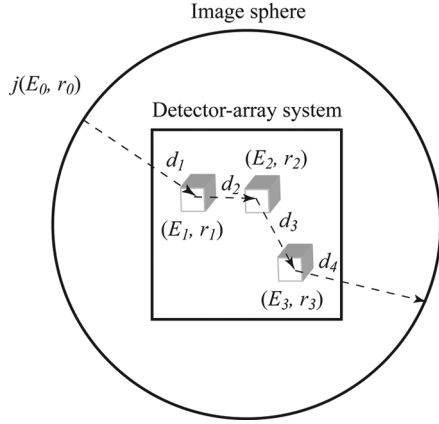


Fig. 1. A three-interaction event  $i(E_1, r_1, E_2, r_2, E_3, r_3)$  is created by a photon from energy and direction  $j(E_0, r_0)$  in the image sphere.

$i$ , a series of energy depositions, in the detector array. The detector-array system introduces uncertainty in recorded interaction position and deposited energy due to noise. Then each measurement is binned into a small volume  $\Delta V_i$  around measurement  $i$  due to the digitization from ADC and pixelation of the detector system. Therefore, the system response function can be achieved in three steps:

- 1) The probability density function for a perfect detector-array system can be derived as  $f(\tilde{i}|j)$ , where  $\tilde{i}$  is the real event created by a detected photon from combined energy and direction  $j$ .
- 2) Assuming the measurement uncertainty from the noise follows a Gaussian distribution,  $f(\hat{i}|\tilde{i})$  can be derived, where  $\hat{i}$  is the response of the detector-array system due to the uncertainty from the real event  $\tilde{i}$ .
- 3) The probability is then integrated over the bin volume  $\Delta V_i$  to achieve the system response function.

In other words, the system response function can be calculated by [3]:

$$t_{ij} = \int_{\Delta V_i} d\hat{i} \int f(\hat{i}|\tilde{i})f(\tilde{i}|j) d\tilde{i}. \quad (1)$$

Due to the limitation of the timing resolution of our system, it is challenging to observe the sequence of the interactions in an event. Several algorithms have been developed to determine the interaction sequence with the maximum probability based on the interaction positions and energies [2], [5], [6]. However, the accurate system model should include all possible sequences. In this work, we consider all energetically possible sequences. Each sequence is weighted based on its probability.

Fig. 1 shows the typical process of a three-interaction event. If the distance between the source and the detector array is much larger than the size of the detector array, a single stationary detector-array system cannot estimate the true three-dimensional source position, only the direction of the incident photon. Therefore the sources can be assumed to be located on the surface of an image sphere with a radius  $R$ .  $R$  is much greater than the dimension of the detector array. A photon with energy  $E_0$  originating from  $j$  can be denoted as  $(E_0, r_0)$ , where  $r_0$  is the position of the incident photon on the image sphere. The

photon travels distance  $d_1$  (entering distance) in the detector material before the first Compton-scatter interaction at location  $r_1$  with energy deposition  $E_1$ , which can be described as  $(E_1, r_1)$ . The scattered photon travels distance  $d_2$  in the detector material before the second Compton scatter  $(E_2, r_2)$ . The scattered photon, after the second Compton scatter, travels distance  $d_3$  in the detector material, then has the third interaction  $(E_3, r_3)$ . For the partial energy deposition case, the escaping photon travels distance  $d_4$  (escaping distance) in the detector material before leaving the detector. The measurement of  $\hat{i}$  and  $\tilde{i}$  can be described as  $(\hat{E}_1, \hat{r}_1, \hat{E}_2, \hat{r}_2, \hat{E}_3, \hat{r}_3)$  and  $(\tilde{E}_1, \tilde{r}_1, \tilde{E}_2, \tilde{r}_2, \tilde{E}_3, \tilde{r}_3)$ , respectively. Similarly, a measured four-interaction event  $i$  can be described as  $(E_1, r_1, E_2, r_2, E_3, r_3, E_4, r_4)$ . In a four-interaction case,  $d_1$  and  $d_5$  describe the entering distance and the escaping distance, while  $d_2, d_3$ , and  $d_4$  describe the photon travel distance in material between the first and the second interaction, the second and the third interaction, and the third and the fourth interaction, respectively.

#### A. Probability Density Function for Three-Interaction Events

Using the chain rule,

$$\begin{aligned} f(\tilde{i}|j) &= f(\tilde{E}_1, \tilde{r}_1, \tilde{E}_2, \tilde{r}_2, \tilde{E}_3, \tilde{r}_3, N_3, D|E_0, r_0) \\ &= f(\tilde{E}_1, \tilde{r}_1, \tilde{E}_2, \tilde{r}_2, \tilde{E}_3, \tilde{r}_3, N_3|E_0, r_0, D) \\ &\quad \cdot f(D|E_0, r_0) \\ &= f(\tilde{E}_1, \tilde{r}_1, \tilde{E}_2, \tilde{r}_2, \tilde{r}_3|E_0, r_0, D) \\ &\quad \cdot f(\tilde{E}_3, N_3|E_0, r_0, \tilde{E}_1, \tilde{r}_1, \tilde{E}_2, \tilde{r}_2, \tilde{r}_3, D) \\ &\quad \cdot f(D|E_0, r_0) \end{aligned} \quad (2)$$

where  $D$  denotes that the photon from  $(E_0, r_0)$  is detected by the detector system, and  $N_3$  represents that there are three and only three interactions in this event. According to Maltz [7],  $f(D|E_0, r_0)$  introduces very small variation in the reconstructed image and can be ignored. So,

$$\begin{aligned} f(\tilde{i}|j) &\approx f(\tilde{E}_1, \tilde{r}_1, \tilde{E}_2, \tilde{r}_2, \tilde{r}_3|E_0, r_0, D) \\ &\quad \cdot f(\tilde{E}_3, N_3|E_0, r_0, \tilde{E}_1, \tilde{r}_1, \tilde{E}_2, \tilde{r}_2, \tilde{r}_3, D) \\ &= f(\tilde{E}_1, \tilde{r}_1, \tilde{E}_2, \tilde{r}_2, \tilde{r}_3|E_0, r_0, D) \\ &= \int_0^\infty f(\tilde{E}_1, \tilde{r}_1, \tilde{E}_2, \tilde{r}_2, t_3, \tilde{r}_3|E_0, r_0, D) dt_3 \end{aligned} \quad (3)$$

$$= \int_0^\infty f(\tilde{E}_1, \tilde{r}_1, \tilde{E}_2, \tilde{r}_2, t_3, \tilde{r}_3|E_0, r_0, D) dt_3 \quad (4)$$

where  $t_3$  is the distance that the scattered photon travels in the detector material between the second and the third interaction. We can expand as

$$\begin{aligned} &f(\tilde{E}_1, \tilde{r}_1, \tilde{E}_2, \tilde{r}_2, t_3, \tilde{r}_3|E_0, r_0, D) \\ &= f(\tilde{r}_3|E_0, r_0, \tilde{E}_1, \tilde{r}_1, \tilde{E}_2, \tilde{r}_2, t_3, D) \\ &\quad \cdot f(t_3|E_0, r_0, \tilde{E}_1, \tilde{r}_1, \tilde{E}_2, \tilde{r}_2, D) \\ &\quad \cdot f(\tilde{E}_1, \tilde{r}_1, \tilde{E}_2, \tilde{r}_2|E_0, r_0, D). \end{aligned} \quad (5)$$

The probability that the second scattered photon travels the distance  $t_3$  in the detector material is

$$f(t_3|E_0, r_0, \tilde{E}_1, \tilde{r}_1, \tilde{E}_2, \tilde{r}_2, D) = \mu_{E_0 - \tilde{E}_1 - \tilde{E}_2} e^{-\mu_{E_0 - \tilde{E}_1 - \tilde{E}_2} t_3} \quad (6)$$

where  $\mu_E$  is the linear attenuation coefficient at energy  $E$  for the material. Further,

$$f(\tilde{E}_1, \tilde{r}_1, \tilde{E}_2, \tilde{r}_2 | E_0, r_0, D) = f(\tilde{E}_2 | E_0, r_0, \tilde{E}_1, \tilde{r}_1, \tilde{r}_2, D) f(\tilde{E}_1, \tilde{r}_1, \tilde{r}_2 | E_0, r_0, D). \quad (7)$$

The probability that the second interaction is a Compton event with energy deposition of  $\tilde{E}_2$  is

$$f(\tilde{E}_2 | E_0, r_0, \tilde{E}_1, \tilde{r}_1, \tilde{r}_2, D) = \frac{N}{\mu_{E_0 - \tilde{E}_1}} \frac{d\sigma_c(E_0 - \tilde{E}_1)}{d\Omega} \bigg|_{\tilde{E}_2} \frac{d\Omega}{d\tilde{E}_2} \quad (8)$$

in which  $N$  is the number of nuclei per unit volume, and  $d\sigma_c(E)/d\Omega$  is the differential scattering cross section per solid angle defined by the Klein-Nishina formula [8]. Let  $\theta_{e_2}$  be the second Compton-scattering angle calculated by deposited energies. The solid angle of a cone with an apex angle of  $2\theta_{e_2}$  is

$$\Omega = 2\pi(1 - \cos\theta_{e_2}) = 2\pi \left( -\frac{m_e c^2}{E_0 - \tilde{E}_1} + \frac{m_e c^2}{E_0 - \tilde{E}_1 - \tilde{E}_2} \right) \quad (9)$$

where  $m_e c^2$  is the rest energy of an electron. So,

$$d\Omega = \frac{2\pi m_e c^2}{(E_0 - \tilde{E}_1 - \tilde{E}_2)^2} d\tilde{E}_2. \quad (10)$$

Define  $\tilde{\Omega}_1 = (\tilde{r}_1 - r_0)/|\tilde{r}_1 - r_0|$ ,  $\tilde{\Omega}_2 = (\tilde{r}_2 - \tilde{r}_1)/|\tilde{r}_2 - \tilde{r}_1|$  and  $\tilde{\Omega}_3 = (\tilde{r}_3 - \tilde{r}_2)/|\tilde{r}_3 - \tilde{r}_2|$ , which are the directions of the incident and the scattered photon.  $\theta_{r_1}$  is the angle between  $\tilde{\Omega}_1$  and  $\tilde{\Omega}_2$ .  $\theta_{e_1}$  is the angle determined by the Compton scattering formula:

$$\cos\theta_{e_1} = 1 + \frac{m_e c^2}{E_0} - \frac{m_e c^2}{E_0 - \tilde{E}_1}. \quad (11)$$

According to Xu [3], given that the initial photon is from location  $r_0$  and has an energy of  $E_0$ , the probability that the first interaction deposits energy  $\tilde{E}_1$  at  $\tilde{r}_1$  and the second interaction happens at  $\tilde{r}_2$  is:

$$f(\tilde{E}_1, \tilde{r}_1, \tilde{r}_2 | E_0, r_0, D) = \frac{1}{4\pi R^2} e^{-\mu_{E_0} d_1} N \frac{d\sigma_c(E_0)}{d\Omega} \bigg|_{\tilde{E}_1} \frac{2\pi m_e c^2}{(E_0 - \tilde{E}_1)^2} \cdot \mu_{E_0 - \tilde{E}_1} e^{-\mu_{E_0 - \tilde{E}_1} d_2} \cdot \frac{\delta(\theta_{r_1} - \theta_{e_1})}{2\pi d_2^2 \sin\theta_{e_1}} \quad (12)$$

where  $1/4\pi R^2$  is the geometric attenuation to reach  $\tilde{r}_1$ . Next,

$$f(\tilde{\Omega}_3 | E_0, \tilde{E}_1, \tilde{\Omega}_1, \tilde{E}_2, \tilde{\Omega}_2, D) = \frac{\delta(\theta_{r_2} - \theta_{e_2})}{2\pi \sin\theta_{e_2}} \quad (13)$$

where  $\theta_{r_2}$  is the angle between  $\tilde{\Omega}_2$  and  $\tilde{\Omega}_3$ ,  $\delta(\theta_{r_2} - \theta_{e_2})$  is the Dirac delta function, and  $\theta_{e_2}$  is calculated from the Compton scattering formula

$$\cos\theta_{e_2} = 1 + \frac{m_e c^2}{E_0 - \tilde{E}_1} - \frac{m_e c^2}{E_0 - \tilde{E}_1 - \tilde{E}_2}. \quad (14)$$

Because  $\tilde{\Omega}_1$ ,  $\tilde{\Omega}_2$  and  $\tilde{\Omega}_3$  are defined by  $r_0$ ,  $\tilde{r}_1$ ,  $\tilde{r}_2$  and  $\tilde{r}_3$ , from (13), we have

$$f(\tilde{r}_3 | E_0, r_0, \tilde{E}_1, \tilde{r}_1, \tilde{E}_2, \tilde{r}_2, t_3, D) = \frac{\delta(\theta_{r_2} - \theta_{e_2}) \delta(d_3 - t_3)}{2\pi t_3^2 \sin\theta_{e_2}}. \quad (15)$$

Combining (5), (6), (7), (8), (12), and (15),

$$f(\tilde{E}_1, \tilde{r}_1, \tilde{E}_2, \tilde{r}_2, t_3, \tilde{r}_3 | E_0, r_0, D) = \frac{1}{4\pi R^2} N^2 e^{-\mu_{E_0} d_1 - \mu_{E_0 - \tilde{E}_1} d_2 - \mu_{E_0 - \tilde{E}_1 - \tilde{E}_2} t_3} \frac{d\sigma_c(E_0)}{d\Omega} \bigg|_{\tilde{E}_1} \cdot \frac{d\sigma_c(E_0 - \tilde{E}_1)}{d\Omega} \bigg|_{\tilde{E}_2} \frac{2\pi m_e c^2}{(E_0 - \tilde{E}_1)^2} \frac{2\pi m_e c^2}{(E_0 - \tilde{E}_1 - \tilde{E}_2)^2} \cdot \frac{\delta(\theta_{r_1} - \theta_{e_1}) \delta(\theta_{r_2} - \theta_{e_2})}{2\pi d_2^2 \sin\theta_{e_1}} \frac{\delta(d_3 - t_3)}{2\pi t_3^2 \sin\theta_{e_2}} \mu_{E_0 - \tilde{E}_1 - \tilde{E}_2}. \quad (16)$$

Integrating (16) over  $t_3$ , we can get the following equation, which is the probability that the initial photon ( $E_0, r_0$ ) has the first Compton interaction ( $\tilde{E}_1, \tilde{r}_1$ ), the second Compton interaction ( $\tilde{E}_2, \tilde{r}_2$ ) and the third interaction at location  $\tilde{r}_3$  in the detector-array system.

$$f(\tilde{E}_1, \tilde{r}_1, \tilde{E}_2, \tilde{r}_2, \tilde{r}_3 | E_0, r_0, D) = \int_0^\infty f(\tilde{E}_1, \tilde{r}_1, \tilde{E}_2, \tilde{r}_2, t_3, \tilde{r}_3 | E_0, r_0, D) dt_3 = \frac{1}{4\pi R^2} N^2 e^{-\mu_{E_0} d_1 - \mu_{E_0 - \tilde{E}_1} d_2 - \mu_{E_0 - \tilde{E}_1 - \tilde{E}_2} d_3} \frac{d\sigma_c(E_0)}{d\Omega} \bigg|_{\tilde{E}_1} \cdot \frac{d\sigma_c(E_0 - \tilde{E}_1)}{d\Omega} \bigg|_{\tilde{E}_2} \frac{2\pi m_e c^2}{(E_0 - \tilde{E}_1)^2} \frac{2\pi m_e c^2}{(E_0 - \tilde{E}_1 - \tilde{E}_2)^2} \cdot \frac{\delta(\theta_{r_1} - \theta_{e_1}) \delta(\theta_{r_2} - \theta_{e_2})}{2\pi d_2^2 \sin\theta_{e_1} 2\pi d_3^2 \sin\theta_{e_2}} \mu_{E_0 - \tilde{E}_1 - \tilde{E}_2}. \quad (17)$$

For a three-interaction event, the third interaction can be a photoelectric interaction or a Compton interaction. If the third interaction is a photoelectric interaction,  $E_0 \approx E_1 + E_2 + E_3$ . The probability for the photoelectric interaction depositing energy  $E_3$  is

$$f(\tilde{E}_3, N_3 | \tilde{E}_1, \tilde{r}_1, \tilde{E}_2, \tilde{r}_2, \tilde{r}_3, E_0, r_0, D) = \frac{\sigma_p(\tilde{E}_3) \delta(E_0 - \tilde{E}_1 - \tilde{E}_2 - \tilde{E}_3)}{\sigma_t(\tilde{E}_3)} = \frac{N \sigma_p(\tilde{E}_3) \delta(E_0 - \tilde{E}_1 - \tilde{E}_2 - \tilde{E}_3)}{\mu_{E_0 - \tilde{E}_1 - \tilde{E}_2}} \quad (18)$$

where  $\sigma_p(\tilde{E}_3)$  is the photoelectric cross section at energy  $\tilde{E}_3$ . If the third interaction is a Compton scatter, instead,  $E_0 > E_1 + E_2 + E_3$ . The probability that the scattered photon after the second interaction deposits part of its energy  $\tilde{E}_3$  in the third Compton interaction and the scatter photon travels distance  $d_4$  in the detector material before escaping from the detector-array system is

$$f(\tilde{E}_3, N_3 | \tilde{E}_1, \tilde{r}_1, \tilde{E}_2, \tilde{r}_2, \tilde{r}_3, E_0, r_0, D) = \frac{N}{\mu_{E_0 - \tilde{E}_1 - \tilde{E}_2}} \frac{d\sigma_c(E_0 - \tilde{E}_1 - \tilde{E}_2)}{d\Omega} \bigg|_{\tilde{E}_3} \cdot \frac{2\pi m_e c^2}{(E_0 - \tilde{E}_1 - \tilde{E}_2 - \tilde{E}_3)^2} e^{-\mu_{E_0 - \tilde{E}_1 - \tilde{E}_2 - \tilde{E}_3} d_4}. \quad (19)$$

By combining (2), (18) and (19) above, two equations are possible.

### 1. Three-interaction full-energy-deposition events

$$f(\tilde{i}|j) = f(\tilde{E}_1, \tilde{r}_1, \tilde{E}_2, \tilde{r}_2, \tilde{E}_3, \tilde{r}_3|E_0, r_0, D) \cdot \frac{N\sigma_p(\tilde{E}_3)\delta(E_0 - \tilde{E}_1 - \tilde{E}_2 - \tilde{E}_3)}{\mu_{E_0 - \tilde{E}_1 - \tilde{E}_2}} \quad (20)$$

### 2. Three-interaction partial-energy-deposition events

$$f(\hat{i}|j) = f(\hat{E}_1, \hat{r}_1, \hat{E}_2, \hat{r}_2, \hat{E}_3, \hat{r}_3|E_0, r_0, D) \cdot \frac{N}{\mu_{E_0 - \hat{E}_1 - \hat{E}_2}} \frac{d\sigma_c(E_0 - \hat{E}_1 - \hat{E}_2)}{d\Omega} \Bigg|_{\hat{E}_3} \cdot \frac{2\pi m_e c^2}{(E_0 - \hat{E}_1 - \hat{E}_2 - \hat{E}_3)^2} e^{-\mu_{E_0 - \hat{E}_1 - \hat{E}_2 - \hat{E}_3} d_1}. \quad (21)$$

In (20) and (21),  $f(\tilde{E}_1, \tilde{r}_1, \tilde{E}_2, \tilde{r}_2, \tilde{E}_3, \tilde{r}_3|E_0, r_0, D)$  is defined in (17).

## B. Considering the Measurement Uncertainties

The measurement uncertainties will be considered in the following integration.

$$f(\hat{i}|j) = \int f(\hat{i}|\tilde{i})f(\tilde{i}|j) d\tilde{i} = \int f(\hat{E}_1, \hat{r}_1, \hat{E}_2, \hat{r}_2, \hat{E}_3, \hat{r}_3|\tilde{E}_1, \tilde{r}_1, \tilde{E}_2, \tilde{r}_2, \tilde{E}_3, \tilde{r}_3) \cdot f(\tilde{E}_1, \tilde{r}_1, \tilde{E}_2, \tilde{r}_2, \tilde{E}_3, \tilde{r}_3|E_0, r_0, D) dV \quad (22)$$

where  $dV$  is defined by differential elements in  $\tilde{E}_1, \tilde{r}_1, \tilde{E}_2, \tilde{r}_2, \tilde{E}_3$  and  $\tilde{r}_3$ .

All measurements of the energy and the position are assumed to follow Gaussian distributions. Given the true interaction energy deposition and position  $\tilde{E}, \tilde{x}, \tilde{y}, \tilde{z}$  from an ideal detector-array system, the distribution of the probability of observing interaction  $\hat{E}, \hat{x}, \hat{y}, \hat{z}$  is

$$f_E(\hat{E}|\tilde{E}) = \frac{1}{\sqrt{2\pi\sigma_E^2}} e^{-(\hat{E}-\tilde{E})^2/(2\sigma_E^2)} \quad (23)$$

$$f_E(\hat{x}|\tilde{x}) = \frac{1}{\sqrt{2\pi\sigma_x^2}} e^{-(\hat{x}-\tilde{x})^2/(2\sigma_x^2)} \quad (24)$$

$$f_E(\hat{y}|\tilde{y}) = \frac{1}{\sqrt{2\pi\sigma_y^2}} e^{-(\hat{y}-\tilde{y})^2/(2\sigma_y^2)} \quad (25)$$

$$f_E(\hat{z}|\tilde{z}) = \frac{1}{\sqrt{2\pi\sigma_z^2}} e^{-(\hat{z}-\tilde{z})^2/(2\sigma_z^2)}. \quad (26)$$

So,  $f(\hat{E}_1, \hat{r}_1, \hat{E}_2, \hat{r}_2, \hat{E}_3, \hat{r}_3|\tilde{E}_1, \tilde{r}_1, \tilde{E}_2, \tilde{r}_2, \tilde{E}_3, \tilde{r}_3)$  is a joint Gaussian distribution, and

$$\int f(\hat{E}_1, \hat{r}_1, \hat{E}_2, \hat{r}_2, \hat{E}_3, \hat{r}_3|\tilde{E}_1, \tilde{r}_1, \tilde{E}_2, \tilde{r}_2, \tilde{E}_3, \tilde{r}_3) dV = 1. \quad (27)$$

In our system, the position uncertainty from pixelation contributes much more angular error than energy measurement uncertainty, so we assume  $\theta_e$  is constant in this calculation.

If the measurement uncertainty in energy and position is fine enough,  $f(\tilde{E}_1, \tilde{r}_1, \tilde{E}_2, \tilde{r}_2, \tilde{E}_3, \tilde{r}_3|E_0, r_0, D)$  varies little within the scale of the uncertainty. It can be considered as a constant, and  $(\tilde{E}_1, \tilde{r}_1, \tilde{E}_2, \tilde{r}_2, \tilde{E}_3, \tilde{r}_3)$  can be replaced by  $(\hat{E}_1, \hat{r}_1, \hat{E}_2, \hat{r}_2, \hat{E}_3, \hat{r}_3)$ . This approximation is valid for the partial-energy-deposition case. However, in the full-energy-deposition case, the delta function  $\delta(E_0 - \tilde{E}_1 - \tilde{E}_2 - \tilde{E}_3)$  in (20) will not vary slowly and has to be calculated separately.

### 1. Three-interaction full-energy-deposition events

$$f(\hat{i}|j) \approx f(\hat{E}_1, \hat{r}_1, \hat{E}_2, \hat{r}_2, \hat{E}_3, \hat{r}_3|E_0, r_0, D) \frac{N\sigma_p(\hat{E}_3)}{\mu_{E_0 - \hat{E}_1 - \hat{E}_2}} \cdot \int \int \int \delta(E_0 - \hat{E}_1 - \hat{E}_2 - \hat{E}_3) \frac{1}{\sqrt{2\pi} \sigma_{E_1} \sigma_{E_2} \sigma_{E_3}} \cdot e^{[-(\hat{E}_1 - \tilde{E}_1)^2/(2\sigma_{E_1}^2) - (\hat{E}_2 - \tilde{E}_2)^2/(2\sigma_{E_2}^2) - (\hat{E}_3 - \tilde{E}_3)^2/(2\sigma_{E_3}^2)]} d\tilde{E}_1 d\tilde{E}_2 d\tilde{E}_3 = f(\hat{E}_1, \hat{r}_1, \hat{E}_2, \hat{r}_2, \hat{E}_3, \hat{r}_3|E_0, r_0, D) \frac{N\sigma_p(\hat{E}_3)}{\mu_{E_0 - \hat{E}_1 - \hat{E}_2}} \cdot \frac{1}{\sqrt{2\pi(\sigma_{E_1}^2 + \sigma_{E_2}^2 + \sigma_{E_3}^2)}} e^{-(E_0 - \hat{E}_1 - \hat{E}_2 - \hat{E}_3)^2/(2(\sigma_{E_1}^2 + \sigma_{E_2}^2 + \sigma_{E_3}^2))} \quad (28)$$

### 2. Three-interaction partial-energy-deposition events

$$f(\hat{i}|j) \approx f(\hat{E}_1, \hat{r}_1, \hat{E}_2, \hat{r}_2, \hat{E}_3, \hat{r}_3|E_0, r_0, D) \frac{N}{\mu_{E_0 - \hat{E}_1 - \hat{E}_2}} \cdot \frac{d\sigma_c(E_0 - \hat{E}_1 - \hat{E}_2)}{d\Omega} \Bigg|_{\hat{E}_3} \frac{2\pi m_e c^2}{(E_0 - \hat{E}_1 - \hat{E}_2 - \hat{E}_3)^2} \cdot e^{-\mu_{E_0 - \hat{E}_1 - \hat{E}_2 - \hat{E}_3} d_1}. \quad (29)$$

## C. Considering the Bin Volume

The probability density function needs to be integrated over the bin volume due to the energy binning and voxelation of the detector volume.

$$t_{ij} = \int_{\Delta V_i} f(\hat{i}|j) d\hat{i} = \int_{\Delta V_i} f(\hat{E}_1, \hat{r}_1, \hat{E}_2, \hat{r}_2, \hat{E}_3, \hat{r}_3|E_0, r_0, D) d\hat{i} \quad (30)$$

where  $d\hat{i} = d\hat{E}_1 d\hat{r}_1 d\hat{E}_2 d\hat{r}_2 d\hat{E}_3 d\hat{r}_3$ .  $\Delta V_i$  is the bin volume around measurement  $i$ .

If the binning volume is small enough that the non-delta function terms change slightly in the bin volume, they can be approximated to be constants and moved out of the integral, and  $(\hat{E}_1, \hat{r}_1, \hat{E}_2, \hat{r}_2, \hat{E}_3, \hat{r}_3)$  can be replaced by  $(E_1, r_1, E_2, r_2, E_3, r_3)$ , the binned and discretized event coordinates.

### 1. Three-interaction full-energy-deposition events

$$t_{ij} \approx \frac{N^3}{4\pi R^2} \frac{1}{2\pi d_2^2 \sin \theta_{e_1} \cdot 2\pi d_3^2 \sin \theta_{e_2}} \cdot e^{-\mu_{E_0} d_1} \frac{d\sigma_c(E_0)}{d\Omega} \Bigg|_{E_1} \frac{2\pi m_e c^2}{(E_0 - E_1)^2}$$

$$\begin{aligned}
& \cdot e^{-\mu_{E_0-E_1} d_2} \frac{d\sigma_c(E_0-E_1)}{d\Omega} \Big|_{E_2} \frac{2\pi m_e c^2}{(E_0-E_1-E_2)^2} \\
& \cdot e^{-\mu_{E_0-E_1-E_2} d_3} \frac{\sigma_p(E_3)}{\sqrt{2\pi(\sigma_{E_1}^2 + \sigma_{E_2}^2 + \sigma_{E_3}^2)}} \\
& \cdot e^{-(E_0-E_1-E_2-E_3)^2 / (2(\sigma_{E_1}^2 + \sigma_{E_2}^2 + \sigma_{E_3}^2))} \\
& \cdot \int_{\Delta V_i} \delta(\theta_{r_1} - \theta_{e_1}) \delta(\theta_{r_2} - \theta_{e_2}) d\hat{i}.
\end{aligned} \tag{31}$$

## 2. Three-interaction partial-energy-deposition events

$$\begin{aligned}
t_{ij} & \approx \frac{N^3}{4\pi R^2} \frac{1}{2\pi d_2^2 \sin \theta_{e_1} \cdot 2\pi d_3^2 \sin \theta_{e_2}} \\
& \cdot e^{-\mu_{E_0} d_1} \frac{d\sigma_c(E_0)}{d\Omega} \Big|_{E_1} \frac{2\pi m_e c^2}{(E_0-E_1)^2} \\
& \cdot e^{-\mu_{E_0-E_1} d_2} \frac{d\sigma_c(E_0-E_1)}{d\Omega} \Big|_{E_2} \frac{2\pi m_e c^2}{(E_0-E_1-E_2)^2} \\
& \cdot e^{-\mu_{E_0-E_1-E_2} d_3} \frac{d\sigma_c(E_0-E_1-E_2)}{d\Omega} \Big|_{E_3} \\
& \cdot \frac{2\pi m_e c^2}{(E_0-E_1-E_2-E_3)^2} \\
& \cdot e^{-\mu_{E_0-E_1-E_2-E_3} d_4} \\
& \cdot \int_{\Delta V_i} \delta(\theta_{r_1} - \theta_{e_1}) \delta(\theta_{r_2} - \theta_{e_2}) d\hat{i}.
\end{aligned} \tag{32}$$

Both cases have the term  $\int_{\Delta V_i} \delta(\theta_{r_1} - \theta_{e_1}) \delta(\theta_{r_2} - \theta_{e_2}) d\hat{i}$ . In our detector-array system, the anode of each detector module is divided into  $11 \times 11$  pixels with pixel pitch of 1.72 mm. The x-y position of the interaction is determined by the anode pixel that collects the electrons. The interaction depth is found by the electron drift time and the cathode-to-anode signal ratio. The depth uncertainty due to digitization is about 0.5 mm. Therefore the bin volume in our system is a rectangular parallelepiped. In order to simplify the calculation, the bin volume for each event is approximated as a sphere with the same volume with a radius of  $R_0$ , as shown in Fig. 2.  $S_1$  is a surface within  $\Delta V_1$ , parallel to  $d_2$ , and containing the first interaction location.  $S_2$  is a curved surface inside of  $\Delta V_2$  that satisfies  $\theta_{e_1} = \theta_{r_1}$ .  $S_3$  is a curved surface within  $\Delta V_3$  that satisfies  $\theta_{e_2} = \theta_{r_2}$ . When  $d_3 \gg R_0$ ,  $S_3$  can be approximated by a plane and  $dz_3 = d_3 \cdot d\theta_{r_2}$ . Similarly,  $S_2$  can be approximated by a plane and  $dz_2 = d_2 \cdot d\theta_{r_1}$ , when  $d_2 \gg R_0$ .  $z_1, z_2$  and  $z_3$  are perpendicular to  $S_1, S_2$  and  $S_3$ , respectively.  $r_0$  is on the back-projection cone defined by  $E_0, E_1, r_1$  and  $r_2$ . The directions not on the back-projection cone will be approximated by a Gaussian function with its standard deviation equal to the angular uncertainty. So,

$$\begin{aligned}
& \int_{\Delta V_i} \delta(\theta_{r_1} - \theta_{e_1}) \delta(\theta_{r_2} - \theta_{e_2}) d\hat{i} \\
& = \Delta E_1 \Delta E_2 \Delta E_3 \int_{\Delta V_1} d\hat{r}_1 \int_{\Delta V_2} d\hat{r}_2 \delta(\theta_{r_1} - \theta_{e_1}) \\
& \cdot \int_{\Delta V_3} d\hat{r}_3 \delta(\theta_{r_2} - \theta_{e_2}) \\
& = \Delta E_1 \Delta E_2 \Delta E_3 \int_{\Delta V_1} d\hat{r}_1 \int_{\Delta V_2} d\hat{r}_2 \delta(\theta_{r_1} - \theta_{e_1}) \int_{-R_0}^{R_0} dz_3
\end{aligned}$$

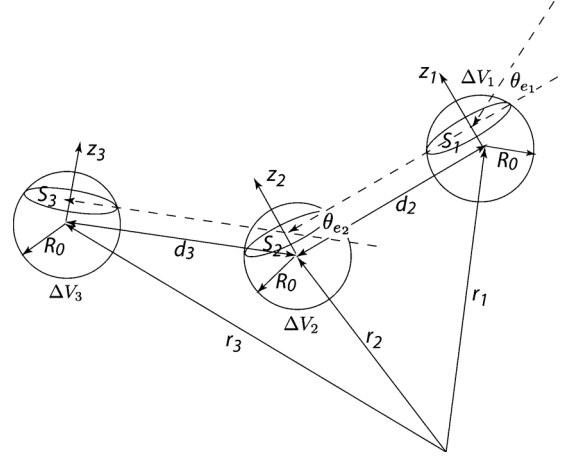


Fig. 2. The binning volumes in the measurement space are approximated by three spheres in calculating the system response function.

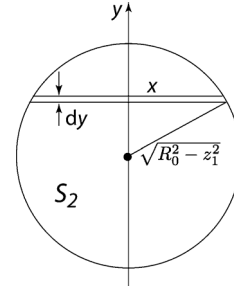


Fig. 3. An illustration of the surface  $S_2$  within  $\Delta V_2$  that satisfies  $\theta_{e_1} = \theta_{r_1}$  for a point in  $\Delta V_1$ .  $y$  crosses the origin of  $S_2$  and is parallel with  $d_2$ .  $x$  is a line within  $S_2$  that is perpendicular to both  $d_2$  and  $y$ .

$$\begin{aligned}
& \cdot \int_{S_3} ds_3 \delta(\theta_{r_2} - \theta_{e_2}) \\
& = \Delta E_1 \Delta E_2 \Delta E_3 d_3 \int_{\Delta V_1} d\hat{r}_1 \int_{\Delta V_2} d\hat{r}_2 \delta(\theta_{r_1} - \theta_{e_1}) S_3 \\
& = \Delta E_1 \Delta E_2 \Delta E_3 d_3 \int_{\Delta V_1} d\hat{r}_1 \int_{-R_0}^{R_0} dz_2 \\
& \cdot \int_{S_2} ds_2 \delta(\theta_{r_1} - \theta_{e_1}) S_3 \\
& = \Delta E_1 \Delta E_2 \Delta E_3 d_2 d_3 \int_{\Delta V_1} S_2 S_3 d\hat{r}_1.
\end{aligned} \tag{33}$$

For each  $z_1$  ( $S_1$  moves along  $z_1$ ), there is a different surface  $S_2$  that satisfies  $\theta_{e_1} = \theta_{r_1}$ . For each line  $x$  with a width  $dy$  in  $S_2$ , shown in Fig. 3, there is a different  $S_3$  which satisfies  $\theta_{e_2} = \theta_{r_2}$ . From geometry, for a specific  $z_1$  and  $y$ , we can calculate that the area of  $S_3$  is  $\pi(R_0^2 - (z_1 \cos \theta_{e_2} + y \sin \theta_{e_2})^2)$  and  $x = 2\sqrt{R_0^2 - z_1^2 - y^2}$ . Therefore,

$$\begin{aligned}
& \int_{\Delta V_i} \delta(\theta_{r_1} - \theta_{e_1}) \delta(\theta_{r_2} - \theta_{e_2}) d\hat{i} \\
& = \Delta E_1 \Delta E_2 \Delta E_3 d_2 d_3 \int_{-R_0}^{R_0} dz_1 \pi(R_0^2 - z_1^2) \\
& \cdot \int_{-\sqrt{R_0^2 - z_1^2}}^{\sqrt{R_0^2 - z_1^2}} dy 2\sqrt{R_0^2 - z_1^2 - y^2} \\
& \cdot \pi(R_0^2 - (z_1 \cos \theta_{e_2} + y \sin \theta_{e_2})^2) \\
& = \Delta E_1 \Delta E_2 \Delta E_3 d_2 d_3 \pi^3 R_0^7 \frac{92 + 4 \cos(2\theta_{e_2})}{105}.
\end{aligned} \tag{34}$$

#### D. System Response Function for Three-Interaction Events

Combining (31), (32) with (34), the two cases are

##### 1. Three-interaction full-energy-deposition events

$$\begin{aligned}
 t_{ij} = & \frac{92 + 4 \cos(2\theta_{e_2})}{105} \frac{\Delta E_1 \Delta E_2 \Delta E_3 N^3 R_0^7}{16R^2 \cdot d_2 \sin \theta_{e_1} \cdot d_3 \sin \theta_{e_2}} \\
 & \cdot e^{-\mu_{E_0} d_1} \frac{d\sigma_c(E_0)}{d\Omega} \Bigg|_{E_1} \frac{2\pi m_e c^2}{(E_0 - E_1)^2} \\
 & \cdot e^{-\mu_{E_0-E_1} d_2} \frac{d\sigma_c(E_0 - E_1)}{d\Omega} \Bigg|_{E_2} \frac{2\pi m_e c^2}{(E_0 - E_1 - E_2)^2} \\
 & \cdot e^{-\mu_{E_0-E_1-E_2} d_3} \\
 & \cdot \frac{\sigma_p(E_3)}{\sqrt{2\pi(\sigma_{E_1}^2 + \sigma_{E_2}^2 + \sigma_{E_3}^2)}} \\
 & \cdot e^{-(E_0-E_1-E_2-E_3)^2 / (2(\sigma_{E_1}^2 + \sigma_{E_2}^2 + \sigma_{E_3}^2))}. \quad (35)
 \end{aligned}$$

##### 2. Three-interaction partial-energy-deposition events

$$\begin{aligned}
 t_{ij} = & \frac{92 + 4 \cos(2\theta_{e_2})}{105} \frac{\Delta E_1 \Delta E_2 \Delta E_3 N^3 R_0^7}{16R^2 \cdot d_2 \sin \theta_{e_1} \cdot d_3 \sin \theta_{e_2}} \\
 & \cdot e^{-\mu_{E_0} d_1} \frac{d\sigma_c(E_0)}{d\Omega} \Bigg|_{E_1} \frac{2\pi m_e c^2}{(E_0 - E_1)^2} \\
 & \cdot e^{-\mu_{E_0-E_1} d_2} \frac{d\sigma_c(E_0 - E_1)}{d\Omega} \Bigg|_{E_2} \frac{2\pi m_e c^2}{(E_0 - E_1 - E_2)^2} \\
 & \cdot e^{-\mu_{E_0-E_1-E_2} d_3} \frac{d\sigma_c(E_0 - E_1 - E_2)}{d\Omega} \Bigg|_{E_3} \\
 & \cdot \frac{2\pi m_e c^2}{(E_0 - E_1 - E_2 - E_3)^2} \\
 & \cdot e^{-\mu_{E_0-E_1-E_2-E_3} d_4}. \quad (36)
 \end{aligned}$$

The definitions of the variables can be found in Table I.

#### E. Simplified System Response Function of Three-Interaction Events for Combining With Other Events

The iterative list-mode MLEM algorithm is performed using [9]–[11]

$$\lambda_j^{n+1} = \frac{\lambda_j^n}{s_j} \sum_{i=1}^I \frac{t_{ij}}{\sum_k t_{ik} \lambda_k^n} \quad (37)$$

where  $\lambda_j^n$  is the estimated intensity in the direction and energy  $j$  at the  $n$ th iteration. The sensitivity  $s_j$  is the detection probability of a gamma ray emitted from  $j$ .  $I$  is the total number of events used in the reconstruction.  $t_{ij}$  is the system response function for event  $i$  from a detected photon  $j$ . For a particular event,  $t_{ij}$  appears in both the numerator and the denominator of (37), so the constant terms for this event will cancel. For a certain event in a specific system,  $\Delta E_1$ ,  $\Delta E_2$ ,  $\Delta E_3$ ,  $N$ ,  $R_0$ ,  $R$  are constant so can be canceled.  $d_2$ ,  $d_3$ ,  $\sin \theta_{e_1}$  and  $\sin \theta_{e_2}$  cannot be canceled because they are not the same for different sequences of one event.  $(92 + 4 \cos(2\theta_{e_2}))/105$  introduces

TABLE I  
DEFINITIONS OF VARIABLES

Variables	Definitions
$E_0$	incident photon energy
$E_1, E_2, E_3$	measured energy depositions
$d_1$	photon entering distance through detector material
$d_2, d_3$	photon in-material travel distance between the first and the second, the second and the third interaction
$d_4$	escaping distance though detector material in partial-energy deposition case
$\mu_E$	linear attenuation coefficient at energy $E$ for the detector material
$\sigma_p(E), \sigma_c(E)$	photoelectric and Compton-scatter cross sections at energy $E$
$\frac{d\sigma_c}{d\Omega}  _E$	Klein-Nishina differential scattering cross-section for depositing energy $E$
$\theta_{e_1}, \theta_{e_2}$	the first and second scattering angles determined using deposited energies and the Compton-scatter formula for the interaction indicated in the subscript
$\sigma_E$	uncertainty in recorded energy
$N$	number of nuclei per unit volume
$R_0$	radius of the sphere with the same volume as the pixelation and the depth uncertainty volume
$m_e c^2$	rest mass energy of an electron

only very small variation in the reconstructed image and can be considered constant and ignored.

The simplified system response functions that can be used for deconvolving a single image with all possible sequences of a particular events and events with other numbers of interaction are:

##### 1. Three-interaction full-energy-deposition events

$$\begin{aligned}
 t_{ij} = & \left[ e^{-\mu_{E_0} d_1} \frac{d\sigma_c(E_0)}{d\Omega} \Bigg|_{E_1} \frac{1}{(E_0 - E_1)^2} \right] \\
 & \cdot \left[ e^{-\mu_{E_0-E_1} d_2} \frac{1}{d_2 \sin \theta_{e_1}} \right] \\
 & \cdot \left[ \frac{d\sigma_c(E_0 - E_1)}{d\Omega} \Bigg|_{E_2} \frac{1}{(E_0 - E_1 - E_2)^2} \right] \\
 & \cdot \left[ e^{-\mu_{E_0-E_1-E_2} d_3} \frac{1}{d_3 \sin \theta_{e_2}} \right] \\
 & \cdot \frac{\sigma_p(E_3)}{\sqrt{2\pi(\sigma_{E_1}^2 + \sigma_{E_2}^2 + \sigma_{E_3}^2)}} \\
 & \cdot e^{-(E_0-E_1-E_2-E_3)^2 / (2(\sigma_{E_1}^2 + \sigma_{E_2}^2 + \sigma_{E_3}^2))}. \quad (38)
 \end{aligned}$$

##### 2. Three-interaction partial-energy-deposition events

$$t_{ij} = \left[ e^{-\mu_{E_0} d_1} \frac{d\sigma_c(E_0)}{d\Omega} \Bigg|_{E_1} \frac{1}{(E_0 - E_1)^2} \right]$$

$$\begin{aligned}
& \cdot \left[ e^{-\mu_{E_0-E_1} d_2} \frac{1}{d_2 \sin \theta_{e_1}} \right. \\
& \left. \frac{d\sigma_c(E_0 - E_1)}{d\Omega} \Bigg|_{E_2} \frac{1}{(E_0 - E_1 - E_2)^2} \right] \\
& \cdot \left[ e^{-\mu_{E_0-E_1-E_2} d_3} \frac{1}{d_3 \sin \theta_{e_2}} \right. \\
& \left. \frac{d\sigma_c(E_0 - E_1 - E_2)}{d\Omega} \Bigg|_{E_3} \frac{2\pi m_e c^2}{(E_0 - E_1 - E_2 - E_3)^2} \right] \\
& \cdot e^{-\mu_{E_0-E_1-E_2-E_3} d_4} \dots
\end{aligned} \quad (39)$$

The simplified (38) and (39) are written in a modular way following the interaction sequence. The first square bracket in both equations represents the process of a photon entering the detector-array system and interacting by Compton scattering. The second square bracket in both equations represents the process that the scattered photon penetrates the detector material towards the second interaction location and Compton scatters the second time. The third square bracket in the full-energy deposition case, (38), represents the process that the scattered photon penetrates the detector material towards the third interaction location and deposits all its energy. The third square bracket in the partial-energy deposition case, (39), represents the process that the scattered photon penetrates the detector material towards the third interaction location, Compton scatters the third time, and then escapes from the detector array.

### III. SYSTEM RESPONSE FUNCTION FOR EVENTS WITH ANY NUMBER OF INTERACTIONS

The system response functions for events with any number of interactions can be extrapolated by changing and adding probability modules which represent the additional physics of penetrations and interactions to (38) and (39).

#### 1. n-interaction full-energy-deposition events

$$\begin{aligned}
t_{ij} = & \frac{1}{d_2 \sin \theta_{e_1} \cdot d_3 \sin \theta_{e_2} \cdot \dots \cdot d_n \sin \theta_{e_{n-1}}} \\
& \cdot e^{-\mu_{E_0} d_1} \frac{d\sigma_c(E_0)}{d\Omega} \Bigg|_{E_1} \frac{1}{(E_0 - E_1)^2} \\
& \cdot e^{-\mu_{E_0-E_1} d_2} \frac{d\sigma_c(E_0 - E_1)}{d\Omega} \Bigg|_{E_2} \frac{1}{(E_0 - E_1 - E_2)^2} \\
& \dots \\
& \cdot e^{-\mu_{E_0-E_1-E_2-\dots-E_{n-1}} d_n} \\
& \cdot \frac{\sigma_p(E_n)}{\sqrt{2\pi(\sigma_{E_1}^2 + \sigma_{E_2}^2 + \sigma_{E_3}^2 + \dots + \sigma_{E_n}^2)}} \\
& \cdot e^{-(E_0-E_1-E_2-E_3-\dots-E_n)^2/(2(\sigma_{E_1}^2 + \sigma_{E_2}^2 + \sigma_{E_3}^2 + \dots + \sigma_{E_n}^2))}.
\end{aligned} \quad (40)$$

#### 2. n-interaction partial-energy-deposition events

$$t_{ij} = \frac{1}{d_2 \sin \theta_{e_1} \cdot d_3 \sin \theta_{e_2} \cdot \dots \cdot d_n \sin \theta_{e_{n-1}}}$$

$$\begin{aligned}
& \cdot e^{-\mu_{E_0} d_1} \frac{d\sigma_c(E_0)}{d\Omega} \Bigg|_{E_1} \frac{1}{(E_0 - E_1)^2} \\
& \cdot e^{-\mu_{E_0-E_1} d_2} \frac{d\sigma_c(E_0 - E_1)}{d\Omega} \Bigg|_{E_2} \frac{1}{(E_0 - E_1 - E_2)^2} \\
& \dots \\
& \cdot e^{-\mu_{E_0-E_1-E_2-\dots-E_{n-1}} d_n} \\
& \frac{d\sigma_c(E_0 - E_1 - E_2 - \dots - E_{n-1})}{d\Omega} \Bigg|_{E_n} \\
& \frac{2\pi m_e c^2}{(E_0 - E_1 - E_2 - \dots - E_n)^2} \\
& \cdot e^{-\mu_{E_0-E_1-E_2-\dots-E_n} d_{n+1}}.
\end{aligned} \quad (41)$$

Particularly, for single-interaction events, the system response functions are:

#### 1. Single-interaction full-energy-deposition events

$$t_{ij} = e^{-\mu_{E_0} d_1} \frac{\sigma_p(E_1)}{\sqrt{2\pi\sigma_{E_1}^2}} e^{-(E_0-E_1)^2/(2\sigma_{E_1}^2)}. \quad (42)$$

#### 2. Single-interaction partial-energy-deposition events

$$t_{ij} = e^{-\mu_{E_0} d_1} \frac{d\sigma_c(E_0)}{d\Omega} \Bigg|_{E_1} \frac{2\pi m_e c^2}{(E_0 - E_1)^2} e^{-\mu_{E_0-E_1} d_2}. \quad (43)$$

(42) and (43) can also be derived without using the approximation of a spherical pixelation-binning volume.

In order to perform the maximum-likelihood deconvolution for single-interaction events, the attenuation distance  $d_1$  and  $d_2$  have to be calculated for every direction for every event. This calculation is very computationally intensive. Compared to multiple-interaction events, single-interaction events provide poorer angular resolution in the reconstructed image due to less concentrated directional information. The source can be located at any direction for a single-interaction event, but it can only be located on a small set of Compton cones for a multiple-interaction event. The image from single-interaction events solely depends on the penetration distance of the photon; hence, it is largely influenced by the geometry and nonuniform detector response.

### IV. PERFORMANCE

In this section, a measurement of three different radioactive sources is used to examine the imaging performance of the MLEM algorithm (37) using the new system response functions derived in this paper. In addition, multiple repetitions of an experiment with a single source are performed to find the statistical uncertainty in these maximum-likelihood deconvolution results. Due to the reasons described in the previous section, single-interaction events are not used in the reconstructions. In this section, two-, three- and four-interaction events are used in the deconvolutions.

For each experiment two algorithms are performed. First, deconvolution is done in a combined spatial and energy space using the full system model considering both full-energy- and



Fig. 4. The spatial deconvolved image from a simultaneous measurement with Cs-137, Na-22, and Co-60 sources, overlaid on an optical panoramic image. The images for energy windows around the primary emission lines of Cs-137, Na-22, and Co-60 are shown in red, green, and blue, respectively.

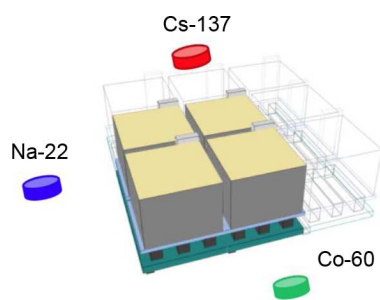


Fig. 5. A diagram of the source arrangement for a measurement with Cs-137, Na-22 and Co-60 sources.

partial-energy-depositions; second, a simplified spatial-only deconvolution only using the full-energy case is also performed. For this spatial-only maximum-likelihood deconvolution, energy windows around the photopeaks are used to select the full-energy-deposition events that match the photopeak-only system model. No sensitivity image is used in this simplified deconvolution method since reconstructed intensities will be skewed anyway due to the Compton continuum from higher energies.

The detector array consisted of four  $2\text{ cm} \times 2\text{ cm} \times 1.5\text{ cm}$  CdZnTe detectors. Since this array was designed for testing purposes, the detectors used had relatively poor spectroscopic performance and uniformity compared to other detectors we have tested. The full width at half maximum (FWHM) energy resolution at 662 keV was 1.07% for single-pixel events from the whole array.

#### A. Maximum-Likelihood Expectation-Maximization Image Reconstruction Using Multiple-Interaction Events

A measurement was performed with three sources in three different directions: a  $14\text{-}\mu\text{Ci}$  Cs-137 30 cm away from the center of the detector array, a  $24\text{-}\mu\text{Ci}$  Na-22 46 cm away from the center of the detector array and a  $2\text{-}\mu\text{Ci}$  Co-60 9 cm away from the center of the detector array, as shown in Fig. 5.

First, maximum-likelihood spatial deconvolutions were performed in energy windows for each of the three sources: 460 keV to 560 keV for Na-22, 600 keV to 700 keV for Cs-137

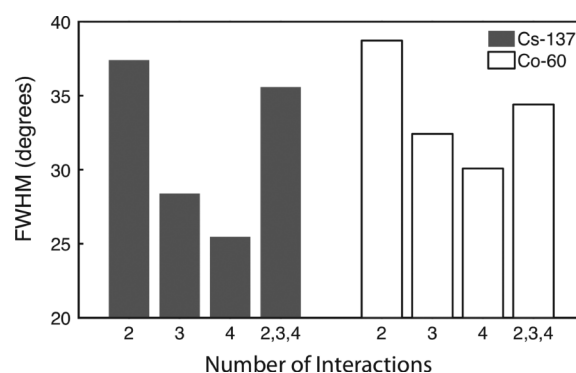


Fig. 6. The comparison of the spatial FWHM in the first iteration of MLEM reconstruction with 500 two-interaction, three-interaction, and four-interaction events individually and 500 combined two-, three-, and four-interaction events from a Cs-137 and a Co-60 source. For the Cs-137 source, the reconstructed events were selected with total energy between 620 keV and 680 keV. For the Co-60 source, the reconstructed events were selected with total energy between 1140 keV and 1350 keV.

and 1100 keV to 1200 keV for Co-60. In the energy window from 1100 keV to 1200 keV, there were 9405 single-interaction events, 35,331 two-interaction non-charge-sharing events, 28,402 three-interaction non-charge-sharing events and 12,044 four-interaction non-charge-sharing events. Therefore, including three- and four-interaction events with two-interaction events increased imaging efficiency by 110%. Fig. 4 shows the superposition of the maximum-likelihood spatial-only deconvolution image from each energy window with a panoramic picture of the laboratory. The image was reconstructed with a  $180 \times 180$  mesh, and the expectation-maximization algorithm was performed with 25 iterations. The reconstructed image from each energy window is shown in a different color. The hotspots in the image are located in the correct source directions.

In another reconstruction, Fig. 6 shows the angular FWHM from each of the image hotspots by using spatial-only deconvolution method with two-, three-, and four-interaction events individually and combined. Fig. 6 is from the first iteration of the deconvolution, starting with a uniform image, using 500

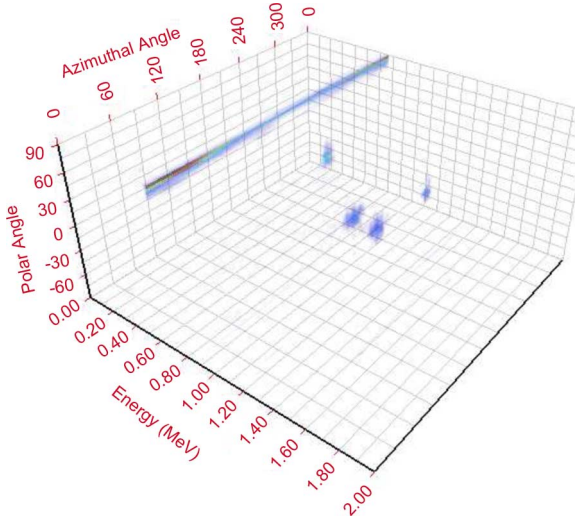


Fig. 7. Reconstructed energy-image using maximum-likelihood deconvolution in a combined spatial and energy domain with the three-source measurement in Fig. 5.

non-charge-sharing events in each reconstruction. The first iteration of the deconvolution is equivalent to the simple back-projection image where the blur is introduced by the position and energy resolution of the detector-array system. In Fig. 6, the width of the hotspot decreases as the number of interactions increases due to less interaction-sequence ambiguity [5]. Compared to the Cs-137 measurement, the angular FWHM from combined two-, three-, and four-interaction events from a Co-60 source is closer to the FWHM from only four-interaction events, due to the fact that four-interaction events are more common in higher-energy events. These relative widths persist through iterations.

Fig. 7 is a three-dimensional view of the results from the maximum-likelihood deconvolution in a combined spatial and energy domain using both the full- and partial-energy-deposition model. The reconstruction was performed with non-charge-sharing two-, three-, and four-interaction events in an energy range of 0 MeV to 2 MeV. The  $4\pi$  spatial domain was divided into a  $64 \times 64$  mesh and the energy domain was divided into 500 energy bins. The sensitivity image used in this deconvolution was calculated from a Monte-Carlo simulation [3]. The three axes are the dimensions of energy, polar angle and azimuthal angle. The intensity in each image voxel is the estimated incident intensity of photons from each incident direction and energy. In the reconstructed image, the hot regions are located in the energy range of 660 keV to 664 keV in the Cs-137 direction, 508 keV to 512 keV and 1272 keV to 1276 keV in the Na-22 direction, and 1172 keV to 1176 keV and 1332 keV to 1336 keV in the Co-60 direction. From this three-dimensional view, it can be seen that the results from this deconvolution algorithm using both the full- and the partial-energy deposition model give the source direction at the peak energies as well as the incident spectrum for each direction. As in the simplified deconvolution case, a larger fraction of the events were used in the reconstruction by including three- and four-interaction events in the deconvolution; the deconvolved spectra preserve the same Compton-continuum-free property as only using two-interaction events.

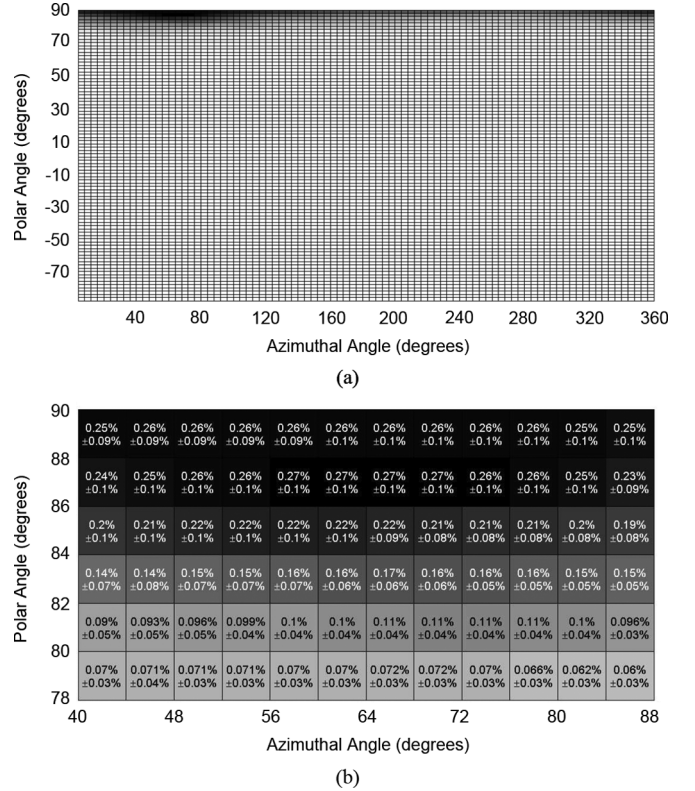


Fig. 8. (a) The reconstructed image from 1000 photopeak events from a Cs-137 source placed almost in the cathode direction (near polar angle of 90 degrees) of the detector array. (b) A detail of the hot region (polar angle of 78 degrees to 90 degrees and azimuthal angle of 40 degrees to 88 degrees). The mean and the standard deviation of the number of counts for each pixel after 20 iteration is shown in each pixel as a percentage of the total image value.

### B. Statistical Uncertainty of the Deconvolution

Fig. 8 shows the average reconstructed image using the maximum-likelihood deconvolution in the spatial domain with 1000 non-charge-sharing two-, three-, and four-interaction photopeak events from a measurement with a Cs-137 source after 20 iterations. Fig. 8 shows the full reconstructed image. It is clear that the point source can be found in the detector array's cathode direction at the top of the image. This experiment was repeated 20 times. After 20 iterations, the total image value within 15 degrees of the cathode direction is on average more than 870 counts. Since the maximum-likelihood expectation-maximization algorithm conserves the total number of counts, more than 87% of the 1000 reconstructed events were located around the correct direction after 20 iterations. Fig. 8(a) shows the percentage mean and the standard deviation of the image value in each pixel around the source direction.

The same method was used to find the uncertainty when deconvolving in both energy and spatial domains with the full system model. A single Cs-137 source was measured, and 1000 non-charge-sharing two-, three-, and four-interaction events were used in the reconstruction. The image was divided into a  $18 \times 18$  mesh, and each energy bin was 4 keV wide. This experiment was performed 20 times. Fig. 9 shows the mean deconvolved spectrum in the source direction and the standard deviation from repetitions. The centroid of the peak is  $662.4 \text{ keV} \pm 0.9 \text{ keV}$ .

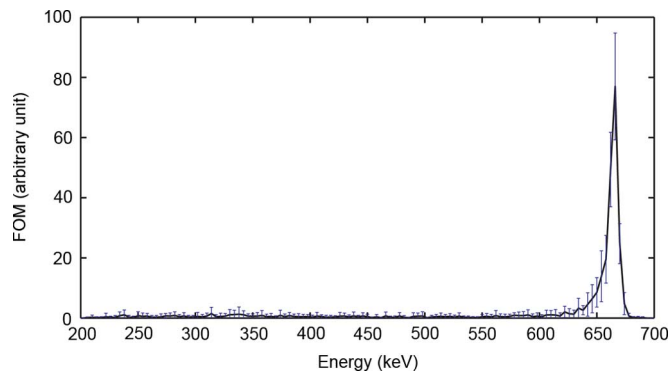


Fig. 9. The mean and the standard deviation of each energy bin in the deconvolved spectrum for the source direction by using the maximum-likelihood deconvolution in a combined spatial and energy domain with 25 iterations for 1000 non-charge-sharing two-, three, and four-interaction events. 20 repetitions are used to calculate the mean and standard deviation.

## V. CONCLUSION

The system response function from 3D-position-sensitive gamma-ray detectors can be established as a function of both energy and direction; therefore, the deconvolved result shows the spatial distribution for each incident energy as well as the incident spectrum for each direction.

Due to the increased volume of each CdZnTe detector module and the new array configuration, the fraction of events with higher number of interactions is increased. In order to make use of these events and improve the imaging efficiency at higher energies, the analytical derivation of the system response was extended to three-interaction events and further extrapolated to events with any number of interactions. By combining single-, two-, three- and more-interaction events in the maximum-likelihood expectation-maximization deconvolution in the spatial and combined spatial-energy domains, all non-charge-sharing events can be used in the reconstruction. In addition, these derivations are applied to an array system.

The experimental results demonstrated that by using the newly derived system response functions, the deconvolved

image from two-, three- and four-interaction events located the source direction, and the deconvolved spectra were free of Compton continuum. By including three- and four-interaction events in the reconstruction, the imaging efficiency was increased by 110% for a Co-60 source, and the angular FWHM was improved as well.

This algorithm is not limited to CZT material or the design of our detector; it can be applied to any gamma-ray detector system that has the capability of providing 3D interaction location and energy deposition for each interaction.

## REFERENCES

- [1] D. Xu, Z. He, and F. Zhang, "4 $\pi$  Compton imaging with single 3D position sensitive CdZnTe detector," *Proc. SPIE*, vol. 5540, pp. 144–155, 2004.
- [2] C. E. Lehner, Z. He, and F. Zhang, "4 $\pi$  Compton imaging using a 3-D position-sensitive CdZnTe detector via weighted list-mode maximum likelihood," *IEEE Trans. Nucl. Sci.*, vol. 51, no. 4, pp. 1618–1624, Aug. 2004.
- [3] D. Xu and Z. He, "Gamma-ray energy-imaging integrated spectral deconvolution," *Nucl. Instrum. Methods Phys. Res. A*, vol. 574, no. 1, pp. 98–109, 2007.
- [4] D. Xu, "Gamma-Ray Imaging and Polarization Measurement Using 3-D Position-Sensitive CdZnTe Detectors," Ph.D. dissertation, Univ. Michigan, Ann Arbor, 2006.
- [5] R. A. Kroeger, W. N. Johnson, J. D. Kurfess, B. F. Philips, and E. A. Wulf, "Three-Compton telescope: Theory, simulations, and performance," *IEEE Trans. Nucl. Sci.*, vol. 49, no. 4, pp. 1887–1892, Aug. 2002.
- [6] I. Y. Lee, "Gamma-ray tracking detectors," *Nucl. Instrum. Methods Phys. Res. A*, vol. 422, no. 1-3, pp. 195–200, Feb. 1999.
- [7] J. S. Maltz, L. Mihailescu, G. T. Gullberg, D. H. Chivers, J. Rohel, and K. Vetter, "Joint spatio-spectral Compton camera reconstruction algorithm for arbitrary detector geometries," in *Proc. IEEE Nuclear Science Symp. Conf.*, 2009, no. N18-5.
- [8] G. F. Knoll, *Radiation Detection and Measurement*, 4th ed. New York: Wiley, 2010, pp. 50–50.
- [9] A. P. Dempster, N. M. Laird, and D. B. Rubin, "Maximum likelihood from incomplete data via the EM algorithm," *J. Royal Stat. Soc.*, vol. 39, no. 1, pp. 1–38, 1977.
- [10] L. A. Shepp and Y. Vardi, "Maximum likelihood reconstruction for emission tomography," *IEEE Trans. Med. Imag.*, vol. 1, no. 2, pp. 113–122, Oct. 1982.
- [11] L. Parra and H. H. Barrett, "List-mode likelihood: EM algorithm and image quality estimation demonstrated on 2-D pet," *IEEE Trans. Med. Imag.*, vol. 17, no. 2, pp. 228–235, Apr. 1998.